Nature-inspired functional porous materials for low-concentration biomarker detection

(Article begins on next page)

22 July 2024

"Nature-inspired" functional porous materials for low-concentration biomarkers detection

Irene Papiano‡[a,b], Simona De Zio‡[b], André Hofer[c], Marco Malferrari[b], Ignacio Mínguez Bacho[c], Julien Bachmann[c], Stefania Rapino[b], Nicolas Vogel[a], Giulia Magnabosco*[a]

Nanostructuration is a promising tool for enhancing the performance of sensors based on electrochemical transduction. Nanostructured materials allow increasing the surface area of the electrode, and to improve the limit of detection (LOD). In this regard, inverse opals possess ideal features to be used as substrates for developing sensors, thanks to their homogeneous, interconnected pore structure and the possibility to functionalize their surface. However, overcoming the insulating nature of conventional silica inverse opals fabricated via sol-gel processes is a key challenge for their application as electrode materials. In this work, colloidal assembly, atomic layer deposition and selective surface functionalization are combined to design conductive inverse opals as electrode material for novel glucose sensing platforms. An insulating inverse opal scaffold is coated with uniform layers of conducting aluminum zinc oxide and platinum, and subsequently functionalized with glucose oxidase embedded in a polypyrrole layer. The final device can sense glucose at concentrations below 1 nM and is not affected by the presence of the common interferents gluconolactone and pyruvate. The method may be also applied to different conductive materials and enzymes to generate a new class of highly efficient biosensors.

Introduction

Biomarker sensors play a fundamental role in point-of-care diagnostics, allowing patients to obtain life-saving data on demand with minimally invasive procedures. The most relevant example is glucose quantification, which is used multiple times a day by millions of patients with diabetes to monitor the sugar level in their blood and to properly dose the insulin administration.[1] Typical glucometers measure the amount of glucose in the patient's blood exploiting glucose oxidase (GOx) immobilized on a single-use test strip[2] including the electrodes for the electrochemical transduction, which can be easily connected to an electronic device for the signal recording and digitalization. The enzyme oxidizes glucose to gluconolactone, and it is subsequently oxidized back to its original state by oxygen while hydrogen peroxide is produced.[3] Hydrogen peroxide, in turn, is oxidized on the surface of the electrode present in the sensor, which generates an electrical current.[4] This method forces patients to prick their fingers to withdraw a blood drop multiple times a day, causing significant discomfort. Other body fluids, such as sweat or saliva, are an attractive alternative to blood,[5] but they contain significantly less glucose and would thus require a much higher sensor sensitivity to produce a detectable signal.

Nanostructured materials can provide novel approaches for sensor development thanks to their large surface area,[6–10] which allows both for miniaturization of the final device and for the decreasing of the detection limit. Regarding inorganic materials, examples in the literature are mainly based on the use of nanoparticles,[11–13] nanowires,[14] nanotubes[15,16], and nanosheets[17] architectures. Their precise fabrication on a large scale, however, is often complex and expensive,[2] and poses a significant obstacle in their use in real-life applications. Electrochemical biosensing gained growing interest thanks to its flexibility and accuracy, [18] and it is the ideal method to sense glucose thanks to the possibility to generate an electric current from glucose exploiting glucose oxidase.[19] One of the most efficient glucose electrochemical sensor developed so far is based on 'black platinum' grown electrochemically on planar surfaces.[20] In this approach, nanostructured Pt is electrochemically deposited on a surface, generating an electrodic material with a large surface area. Its high surface area and its proficiency in the catalytical oxidation of hydrogen peroxide-one of the products of the glucose oxidation reaction by GOx- allow for the detection of glucose concentrations as low as 10 nM. A promising alternative is to use high surface area, nanostructured materials as the scaffold onto which the active metal is deposited. This strategy makes more efficient use of the active metal, exploits the current and well-assessed knowledge on conventional sensors, and allows for the development of sensors with improved performance.

Nanostructured materials are widespread in nature and they are an excellent source of inspiration for scientists, which, on top of the clever strategies optimized by nature itself, have access to a wider selection of materials to choose from. Inverse opals (IOs) are 3-dimensional porous networks obtained by backfilling a sacrificial colloidal crystal with a desired precursor, which is inspired by the natural opal gem stone and assembled taking advantage of self-assembly, another of the most fascinating natural phenomena. IOs, initially used to replicate the structural coloration occurring in nature both in the inanimate and animate world,[10,21] possess ideal features to be used as materials for sensor development.[9,10,22,23] The order typical of the IO structure poses significant advantages over the use of other porous, less ordered materials such as foams and mesoporous silica since the complete interconnectivity of the pores allows to exploit the whole area for surface-based processes . This characteristic becomes fundamental for sensing applications, as it facilitates the transport of the target analyte to the active surface and improves the signal measured, where the LOD was 5uM.[10,24–26] So far, multiple example of organic IOs for detection of bioanalytes have been developed, with a particular focus on the use of hydrogels. [27–29] Inorganic IOs show increased thermal and mechanical stability compared to organic ones and their surface can be readily functionalized with a range

of chemical or physical methods, including atomic layer deposition (ALD),[30] layer-by-layer deposition,[30] and self-assembled monolayers. [31] Additionally, inorganic IOs can be fabricated easily and reliably using the co-assembly technique, consisting of the simultaneous assembly of the sacrificial particles and the sol-gel precursor of the matrix.[32]

Cao et al. [33] were able to increase the efficiency of glucose detection by immobilizing GOx on titania IOs grown on ITO substrates. Even though the resultant porous framework was not highly ordered, the increased surface area of the IOs allowed the adsorption of GOx with higher efficiency with respect to the analogous plain samples. Therefore, the sensors showed a higher catalytic activity toward glucose oxidation and a higher sensitivity to glucose detection than ordinary titania-modified electrodes.[33] To the best of our knowledge, this was the only attempt to generate inorganic electrochemical glucose biosensors based on IO produced with the sol-gel method. We ascribe this to the difficulties in preparing conductive IOs.

Typical IO fabrication methods rely on sol-gel precursors that solidify around the templating particles. The most abundantly used sol-gel matrix for the fabrication of IOs is silica, which is an insulator. The integration of electrical conduction is typically achieved by the addition of metal or semiconducting particles during the assembly, which, however, leads to problems with mechanical stability and in the preservation of the porous structure of the templating particles.[10,34] Other methods for preparing IOs using conductive materials exploiting atomic layer deposition (ALD) [35–39] or electrochemical deposition [40] are reported in the literature. In particular, ALD can coat the polymer colloidal crystal conformally and completely with the desired inorganic material. Due to the stepwise ALD process, this strategy is expensive and time-consuming. A more elegant approach uses conventional sol-gel IO fabrication followed by a shorter, efficient ALD process to coat the conductive material as a thin layer on top of the silica IO. This approach offers several advantages over the use of full ALD deposition and has so far applied to catalysis,[30,41] photonic[42,43] and biofouling prevention,[44,45] but not for sensing applications.

In this work, we overcome this challenge by separating the structure formation from the integration of the conductive component. We combine the structural regularity typical of silica IOs prepared from colloidal co-assembly,[32] with the conductive properties of aluminum zinc oxide (AZO) deposited with ALD, which enables us to coat the entire interior surface with a homogeneous, thin layer of metal oxide. Finally, we add an ultrathin layer of Pt via ALD as a material-efficient way to introduce the active metal. This strategy allows for the fabrication of conductive Pt-decorated IOs able to efficiently transport electrical current. With respect to fabrication of the IO scaffold with ALD, our 2-step approach combining sol-gel methods and thin ALD coating minimizes the use of expensive materials compared to inverse opal scaffolds formed completely from the active precious metal, and decouples the formation of the porous media, the introduction of conductivity, and the deposition of active material.

As several species can be directly oxidized at the Pt surface, it is necessary to functionalize it with a (bio)molecule that gives the proper selectivity to the detection. By embedding GOx in a polypyrrole layer, we fabricate a glucose sensor based on established transduction strategies with high sensitivity and selectivity.[46] The possibility to fine-tune all these parameters gives our platform unprecedented control over the features of the final device and opens the possibility to apply it to different biomarkers by selecting the appropriate electrodic material-enzyme combination.

Results and discussion

Our biosensor is based on a combination of colloidal self-assembly and precise surface modification steps (Figure 1). First, we use the co-assembly technique to form IOs with well-defined, interconnected and ordered pores on a conductive indium tin oxide (ITO)-coated glass substrate (Figure 1a). Subsequently, we employ ALD to form a continuous, conductive layer of aluminum zinc oxide (AZO) that conformably coats the entire inner surface of the IO (Figure 1b). This step ensures the charge transfer through the 3D structure and the proper current measurement by the potentiostat. Next, we add a thin layer of Pt, using a single ALD deposition cycle (Figure 1c). This step provides the active metal needed to catalyze the oxidation of hydrogen peroxide[47] – the product of the glucose enzymatic oxidation. Both these last two steps are important for the reliable functioning of the device. In fact, using only Pt in the ALD process does not easily form a continuous layer due to its growth in polycrystalline islands.[48–51] In contrast, AZO more readily forms conformal coatings, thereby ensuring an efficient charge transport but it is not as efficient as platinum in catalyzing the electrochemical oxidation of hydrogen peroxide.[52] Additionally, this approach also minimizes the use of expensive Pt and therefore provides a resource-efficient sensor design. Thus, our approach combining sol-gel deposition and ALD is significantly more resource-efficient than a complete
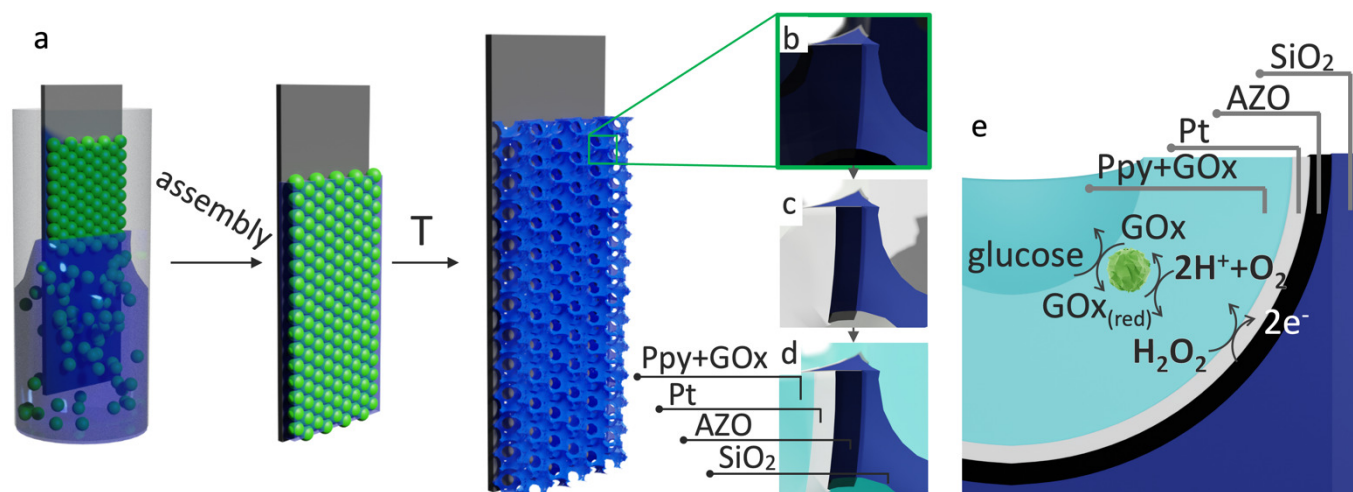
Figure 1. Schematic representation of the preparation of the device. a) Step one: Preparation of a silica inverse opal on an ITO-covered glass slide. b) Step two: AZO deposition over the SiO_2 IO. c) Step three: Pt deposition. d) Step four: electrochemical polymerization of polypyrrole embedding GOx. e) Schematic of the enzymatic reaction taking place in the biosensor.

deposition of the IO components using solely ALD. Finally, we integrate GOx as the enzyme responsible for the selective oxidation of glucose. We use a well-established protocol that relies on embedding the enzyme in a polypyrrole layer, which facilitates the immobilization of GOx and has been shown to improve the selectivity of the device[53] (Figure 1d). In the final device, the electrochemical detection of glucose is achieved as follows (Figure 1e): the reduction of the FAD redox cofactor in the enzyme is promoted by reaction with glucose, which is oxidized to gluconolactone; molecular oxygen regenerates the oxidized form of the FAD group in GOx producing hydrogen peroxide, which is amperometrically assessed at the Pt surface by the application of an anodic potential. Then, the catalytic cycle is repeated.

In the following, we systematically investigate in detail the individual steps needed for the sensor design. We first optimize the electrode porosity and its conductivity. Both parameters are controlled by a combination of two factors: (i) the pore size, which is determined by the diameter of the templating particles; and (ii) the thickness of the conductive layer deposited onto the IO surface to control the flow of charges. Both factors impact on the aperture of the small openings between pores — referred to as necks — that regulate the transport of the chemical species within the inner structure and, thus, the sensitivity of the sensor.[10] Balancing charge conductivity and mass transport through the structure is therefore essential for proper device performance.

We use the co-assembly technique, in which hydrolyzed tetraethyl orthosilicate (TEOS) assembles together with sacrificial templating polymeric particles to form the inverse opal structure. Particles are transported to the drying edge and self-assemble in a well-ordered colloidal crystal. Simultaneously, TEOS as the silica source is also transported to the meniscus and is being integrated into the interstitial sites. Upon calcination the polymeric particles are removed and silica further condense to form a continuous matrix in the interstitial sites of the particles.[32] We produced IOs with pores sizes of 220

nm, 290 nm, 350 nm, and 565 nm, controlled by the diameter of the templating polystyrene colloidal particles [32](Figure SI1). For this specific application, the main goal is to obtain IOs with the most regular morphology achievable, and with a neck size that allows sufficient flow of substances for subsequential functionalization steps, taking into consideration the challenge of diffusion in IOs.[54] Note that as no photonic effect is exploited, the pore size is not limited to dimensions that would interact with light to form structural color, which is a common design criteria for IOs.[10,55] IOs with 350 nm pores showed the lowest number of cracks, the highest pore connectivity, and the highest surface-to-volume ratio at a fixed number of layers to enable comparison. We, therefore, used these IOs in the subsequent experiments.

The next step is the introduction of the conductive AZO and Pt layers using ALD. We chose AZO according to its ability to carry charges at low thickness[56–58] and we vary its thickness via the number of ALD cycles used for its deposition to optimize the conductivity while maintaining pore accessibility. We integrate small amounts of Pt, the active metal responsible for the oxidation of H_2O_2 on the AZO-coated IOs, by performing just 1 cycle of ALD deposition.

Figure 2 compares two different AZO coatings with nominal layer thicknesses of 4 nm and 20 nm, determined by ellipsometry on a reference planar substrate, and a thin Pt layer. The Scanning Electron Microscopy (SEM) images shown in Figure 2a-c indicate that the ALD layer conformally coats the entire surface, as no uncovered patches in the structure are seen. The visual impression of the reduction of pore sizes with increasing AZO layer thickness is corroborated by statistical image analysis, shown in Figure 2 d,e. The dimension of pores is reduced from 277±13 nm in the pristine sample to 262±20 nm for the nominal 4 nm thick AZO film, and to 237±13 nm for the 20 nm AZO film. A similar behavior is observed for the necks[10](Figure 2e), which are reduced from 118±10 nm to an
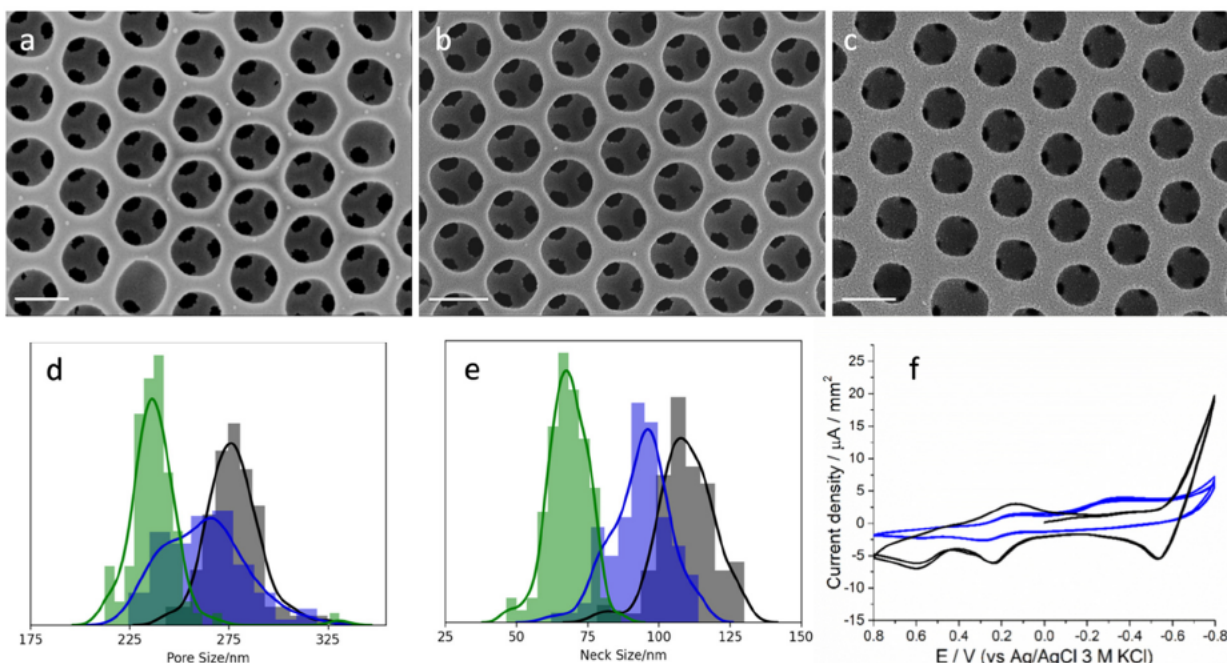
Figure 2. ALD coating of inverse opals with aluminum zinc oxide (AZO). a-c) SEM images of uncoated IO (a), 350 nm pore IOs covered with 4 nm (b) and 20 nm (c) of AZO, underlining the conformal nature of the ALD coating. Scale bar is 300 nm. d,e) size distribution of pores (d) and necks (e) for uncoated IO (black), and IO coated with 4 nm (blue) or 20 nm (green) AZO. f) Cyclic voltammetry of IOs with 4 nm (black) and 20 nm (blue) AZO, FeMeOH 2 mM in phosphate buffer, scan rate is 20 mV/s.

opening diameter of 94±10 nm and 68±7 nm for the 4 nm and 20nm coating, respectively.

We then use cyclic voltammetry to characterize the electrochemical behavior of the material and thus assess its conductivity. Figure 2f shows the cyclic voltammograms of both coated samples, showing a clear increase in current density for the thinner AZO coating (black line) compared to the thicker AZO coating (blue lines) (Details in SI). We may ascribe this behavior to (i) the reduced resistivity of AZO at lower thicknesses (figure SI2) and (ii) the enhancement of the accessible surface area provided by the interconnected porous network of the IOs coated with a thin oxide layer. Based on this behavior, we choose the IOs coated 4 nm AZO and a thin layer or Pt as the ideal conductive platform.

The SEM image shown as inset in Figure 3a indicates the presence of very small Pt nanoparticles that densely coat the entire surface. This morphology is ideal to fabricate a sensor, as it maximizes the active surface for the electrochemical processes while minimizing the amount of Pt needed in the device. Energy-dispersive X-ray spectroscopy further confirms the presence of Pt, along with Zn from the AZO layer within the sample (Figure 3a, Table SI1).

We then assess the ability of the Pt-containing conductive IOs to electrochemically detect hydrogen peroxide by performing standard addition during a multi-step chronoamperometric measurement (Figure 3b, Figure SI4c, SI5). The data show that the working electrode responds to hydrogen peroxide with concentrations of 50 nM and higher. These measurements demonstrate that the IO electrodes allow for efficient signal transduction of the hydrogen peroxide and can thus work as a direct sensor at lower concentrations than those of standard commercially available glucose biosensors.[18,59]
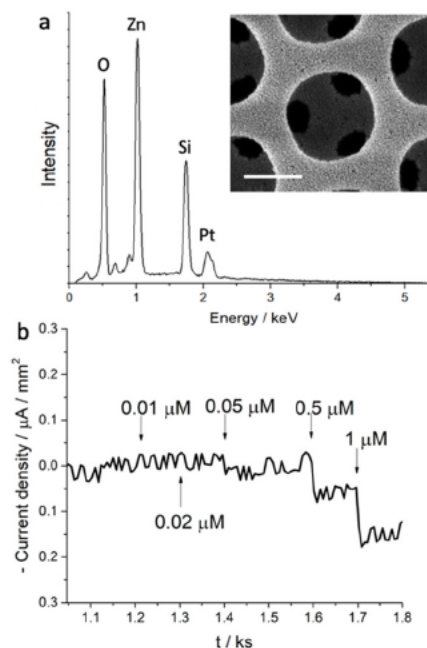

Figure 3. Integration of platinum into the conductive inverse opal architecture. a) EDX confirming the presence of Pt and Zn within the structure, SEM picture showing the Pt island nanostructure as inset. Scale bar is 150 nm. b) Multi-step chronoamperometic measurements of H_2O_2 standard additions on Pt-covered IO. Further addition in Figure SI5. The curves are registered in PBS solution at RT, the reported currents are measured at $E = +0.65$ V vs Ag/AgCl (3 M KCl), after 120 ms from the application of the potential step.
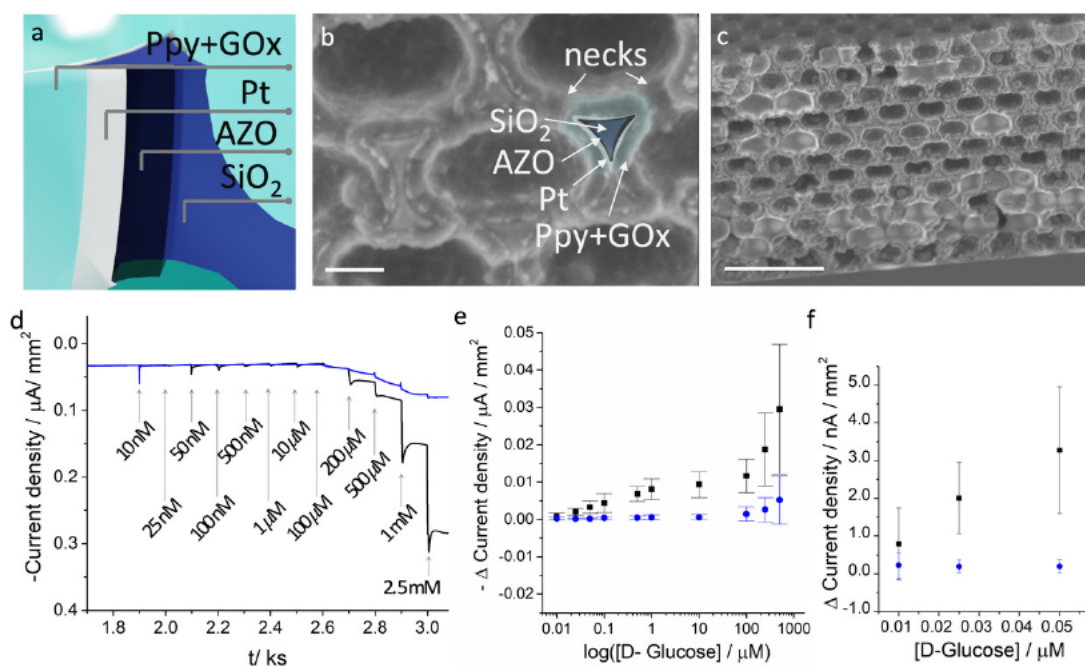
Figure 4. Integration of GOx in a polypyrrole film into the IO architecture and performance as a biosensor. (a) Schematic describing the morphology of the sample. Refer to Figure 1 b-d for further details on the composition of the sensor and to figure SI4 for more details on preparation and macroscopic pictures. (b-c) cross-section SEM images of the final device. The colored inset in (b) identifies the different layers described in (a). Scalebar is (b) 100 nm and (c) 1 μm. (d) Chronoamperometric measurements of standard additions for planar (blue) and IO-based biosensors (black). The curves are registered in PBS solution at RT, E = + 0.65 V vs Ag/AgCl (3 M KCl). The reported behavior is representative of 3 independent measurements per sample. (e-f) Change in current density during glucose standard additions for planar (blue) and IO-based biosensors (black) presented using the logarithmic scale for glucose additions (e) and using the linear scale for the lowest additions (f). Bars represent standard deviations of the measurements. The slope determined for the IO-based biosensor is 7.28×10^{-8} A/uM, while the one for the planar biosensor is 4.85×10^{-9} A/uM. The data are reported using the linear scale for glucose addition in Figure SI6a.

In order to confer the proper selectivity and sensibility toward the electrochemical detection of glucose, GOx, which is responsible for the catalytical oxidation of glucose while producing hydrogen peroxide, needs to be integrated into the device architecture.[2,18] Building on our earlier findings[24], we embed GOx into a polymeric film, which ensures mechanical stability, preserves catalytic activity, and simultaneously improves selectivity.[53,60] For a reliable performance, the enzyme-containing polymer film needs to uniformly coat the entire inner surface of the porous network. To avoid diffusion typical limitations of polymers in the confinement of the nanoporous material, electropolymerization[46,53,60], enabled by the conductive nature of the IO materials, is the best candidate for an efficient, conformal and homogeneous functionalization over the whole surface area of the structure (Figure SI4). In this approach, only small monomer molecules need to diffuse inside the IO, and macromolecules are directly formed on the IO surface from the monomers, facilitating the formation of a homogeneous coating throughout the whole structure. Among the polymers which can be deposited by electropolymerization, polypyrrole possesses the ideal characteristics for IO functionalization. Polypyrrole allows for a single step electrode functionalization route, and thanks to the high water-solubility of the monomer, it does not require the addition of surfactants. These mild polymerization conditions ensure that the GOx functionality is retained during the functionalization procedure.[61]

We previously demonstrated how polypyrrole can efficiently polymerize over Pt surfaces and embed GOx in its matrix without affecting its activity and allowing the generation of charges during the enzymatic reaction. [46,62] When polypyrrole is electropolymerized over the conductive IO surface, a uniform polymer layer penetrates the porous network completely as seen in the SEM micrographs, Figure 4b,c.

The high-resolution SEM image of Figure 4b also shows the pore interconnectivity with open necks bridging individual pores, and all the different layers deposited to form the sensor device. We estimated the quantity of GOx immobilized in the system to be in the range between 1.14×10^{-4} Units/ mm^2 and 1.3×10^{-1} Units/mm^2 (see SI).

We test the performance of the complete IO biosensor device by chronoamperometric calibrations with standard additions of known concentrations of glucose. Figure 4d compares the evolution of current density for the IO-based electrodic material (black lines) and a reference planar electrode (blue lines), and Figures 4e,f show the change in current density for both architectures. For glucose concentration in the range 0.01-1 μM, an increase in sensitivity of 15 times for the IO architecture with respect to a planar biosensor (the slope of the interpolation line of the IO-based sensor is 6.9×10^{-3} μA/μM while it is 1.06×10^{-5} μA/μM for the plain biosensor (see Figure SI6). The limit of detection calculated with the linear regression method for the IO-based sensor, as the conventional way of assessing the performance,[63,64] resulted in a value below 1 nM
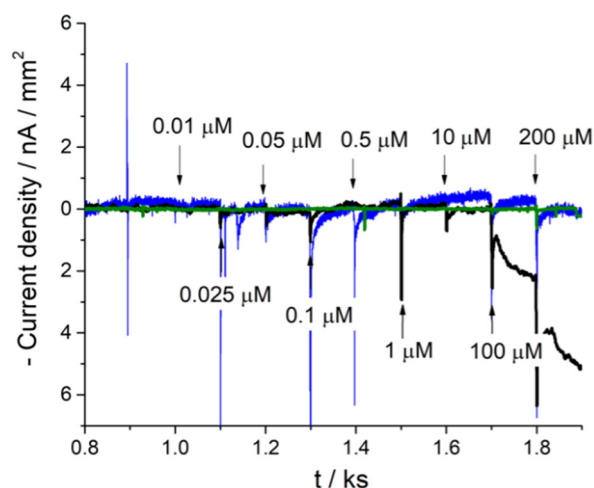
Figure 5. Selective response of the IO-based biosensor. Representative chronoamperometric measurements of standard additions of glucose (black), gluconolactone (blue), and pyruvate (green). The curves are obtained in PBS solution at RT, E=+0.65 V vs Ag/AgCl (3 M KCl).

(Figure SI6), increasing the sensitivity of more than one order of magnitude with respect to the current state of the art.[20] However, we experimentally tested the responses of the biosensors in the glucose concentration range 10 nM- 2.5 mM, which provides a more realistic concentration range for detection. A clear detection by the current change, taking into account the measurement error can be seen from values above 25 nM (Figure 4e).

When compared to IO-based systems, our platform performs significantly better than what previously reported in the literature for ZnO IO sensors, where the LOD was 5 µM.[65]

The low limit of detection, together with the low amount of noble metal needed, make our platform the ideal candidate for glucose sensing.

To prove the selectivity of the final device, we studied the effect for two relevant interferents[66,67] on the current density using chronoamperometry. The selectivity towards glucose in the presence of gluconolactone is of fundamental importance as gluconolactone is the product of glucose oxidation, and its presence can thus not be avoided during sensing. Pyruvate is the product of the glycolysis, which plays a fundamental role in diabetes. [68] As observed in Figure 5, both pyruvate and gluconolactone do not significantly impact the electric signal, thus making our sensor selectively responsive to glucose even in the presence of other biomarkers. We also investigated the stability of the platform over a 72-hour period and under high stressing working conditions (Figure SI7). We tested the sensor at significantly higher glucose concentrations (up to 2.5 mM) than what it would experience in the envisioned applications – the analysis of body fluid with low concentration of glucose (up to 0.5 mM[69]) - and we verified that it is still able to detect changes in current density after that time frame and stress tests. We consider this result to represent the minimum sensitivity retained under stress, as the loss in performance would be decrease when exposed to glucose concentrations in the envisioned range. This is ensuring a high stability especially when thinking to the single use of typical *point-of-care*

solutions. Furthermore, the inorganic components of the electrode can potentially be regenerated with thermal or solvent treatments and re-functionalized with a fresh enzyme solution to allow for multiple uses of the electrode component. These fundamental findings pose the basis for the application of our strategy in real glucose monitoring systems.

Experimental

Inverse Opals preparation. SiO_2 inverse opals (IOs) were generated via the colloidal co-assembly technique on 0.9 cm x 5 cm indium tin oxide (ITO) – coated glass substrates, previously cleaned with O_2 plasma. A mixture of tetraethyl orthosilicate (TEOS), ethanol, and 0.1 M hydrochloric acid (volumetric ratio 1:1.5:1) was stirred for 1 hour at room temperature to pre-hydrolyze TEOS. Then, a 0.1 wt % dispersion of polystyrene colloidal particles and 75 µL of pre-hydrolyzed TEOS solution were added to MilliQ H_2O for a total volume of 12 mL. The substrate was immersed vertically into the solution and placed in an oven equipped with vibration-absorbing rubber plates at 65°C to evaporate the water. During this evaporation process, the convective flows led to the deposition of a composite thin film composed of a close-packed crystal of the polymer colloidal particles with silica-filled interstitial sites. The templating colloidal particles were removed by thermal treatment at 500 °C to produce the IO. The polystyrene colloidal particles with different diameters were synthesized by surfactant-free emulsion polymerization using ammonium persulphate as the initiator and acrylic acid as the comonomer, as described elsewhere.[32,70] All reagents were purchased from Sigma-Aldrich and used without further purification unless stated otherwise.

Coating of conductive materials. The IOs were coated with conductive materials using atomic layer deposition (GEMStar XT 6 reactor, Arradiance). First, aluminum doped zinc oxide (AZO) with a ratio $Al_2O_3/ZnO = 1:20$ was deposited starting from diethylzinc (DEZ 95%, abcr), trimethylaluminium (TMA 97%, abcr) and H_2O at a reaction temperature of 90 °C. The number of deposition cycles was varied to tune the AZO film thickness. Subsequently, platinum was deposited on top by ALD using[71] trimethyl(methylcyclopentadienyl)platinum(IV) (MeCpPtMe$_3$ 98%, abcr) as precursor together with ozone at 220 °C. The nominal thickness and homogeneity on planar substrates (AZO 1 cycle: 4 nm, 5 cycles 20 nm, Pt 1 cycle: 1 nm) was determined on SiO_2 wafers by spectroscopic ellipsometry (SENPro, SENTECH). Due to possible nucleation inhibition the true loading in the porous system can be lower than the nominal value recorded on a planar reference sample.

Planar reference platforms fabrication. To determine what is the effect of the nanostructure on the glucose sensing performances, we prepared sensors on planar surfaces. Here, 0.9 cm x 5 cm indium tin oxide (ITO) – coated glass substrates were first treated with O_2 plasma. We then deposited AZO and Pt as described in the paragraph "**Coating of conductive materials**". The nominal thickness and homogeneity on planar substrates (AZO 1 cycle: 4 nm, 5 cycles 20 nm, Pt 1 cycle: 1 nm) was determined on SiO_2 wafers by spectroscopic ellipsometry (SENPro, SENTECH). The deposition process was carried out

together with the one on IO-based sensors to minimize variations due to the deposition procedure.

Electrochemical instrumentation. The nanostructures were electrochemically characterized by cyclic voltammetry (CV) using a three-electrode system, comprising an Ag/AgCl (3 M KCl) and a Pt wire acting as reference and counter electrode, respectively. The IO surfaces were used as the working electrode after being contacted to the bipotentiostat circuit using a copper stripe. The cyclic voltammograms were recorded at a scan rate of 20 mV/s in the region from −0.8 to 0.8 V vs. Ag/AgCl (3 M KCl). Ferrocenemethanol 2 mM in phosphate buffer (pH 6.9) was used as redox species to characterize the electron transfer properties of the IO-based electrode. Ferrocene methanol 97%, sodium phosphate monobasic and sodium phosphate dibasic were purchased from Merck.

Enzyme layer incorporation. The enzyme glucose oxidase was immobilized on the Pt surface by electropolymerizing a thin polypyrrole (PPy) film in the presence of glucose oxidase, this results in a thin polymer film embedding the enzyme stably adherent to the Pt surface. This GOx/PPy film was prepared via electro-polymerization of 0.15 M pyrrole and 2 mg/mL GOx phosphate buffer solution. A three-electrode configuration consisting of an Ag wire as the quasi-reference electrode (QRE), a Pt wire as the counter electrode and the conductive IO structure as the working electrode was used. The electrochemical cell was covered with silicone rubber to prevent O_2 to diffuse back from the atmosphere into the solution after degassing it: the pyrrole-containing enzymatic solution was inserted into the cell and degassed for 5 minutes with Ar bubbling. Before the polymerization, CVs were recorded to verify the absence of oxygen in solution at a scan rate of 20 mV/s in the region from −0.7 to 0 V *vs.* Ag wire QRE. The electro-polymerization was started under moderate stirring: the film was grown chronoamperometrically at a fixed potential +0.9 V *vs.* Ag wire QRE for approximately 15 minutes. The procedure has been adapted from Soldà et al.[46]. Glucose Oxidase (GOx) type X-S (EC 1.1.3.4. from Aspergillus Niger, Merck) and pyrrole 98 % (Merck) were used as received.

Evaluation of sensor performances. The biosensing performance was evaluated at different stages of the sensor fabrication. The ability of the metal-coated IOs to detect hydrogen peroxide, the response of the enzyme-coated IOs to β-D-glucose, and the selectivity to the analyte against interfering species, such as pyruvate and gluconolactone were studied. These analyses were conducted using chronoamperometric calibrations in phosphate-buffered saline solution (PBS pH 7.4, Lonza) at room temperature.[46] After current equilibration, standard concentrations of the appropriate analyte – H_2O_2, β-D-glucose, pyruvate, or gluconolactone – were added every 100 s. The electric potential of the electrode was kept at E = +0.65 V vs.Ag/ AgCl (3 M KCl) , at which the H_2O_2 oxidation is detected. The curves were treated, and data were processed by employing OriginPro 9.1. Calibration plots reporting electrochemical responses of IO/planar biosensing substrates to analytes additions were obtained by processing amperometric calibration curves: oxidation current before the addition of the analyte was subtracted from the current after each addition (after steady state was reached) obtaining a series of increments that are attributed to the relative analyte concentrations. These resulting current steps are plotted against the concentrations of the analyte in the solution for the addition of interest.

Phosphate-Buffered Saline 1x (pH 7.4) (Microtech), β-D-glucose (Merck), sodium pyruvate (>99%, Merck), δ-Gluconolactone (Merck), Hydrogen Peroxide (30% w/v, Panreac) were used as received.

Scanning electron microscopy observations. The multilayered ALD-coated IO was characterized by scanning electron microscopy (SEM). The images were acquired with a Zeiss Gemini 500 working at 1 kV, equipped with an Inlens detector.

Energy-Dispersive X-ray analysis. We analyzed the elemental composition of the metal-coated IOs built on silicon wafers with a scanning electron microscope Gemini Ultra 55 (Zeiss) combined with an EDX detector (Noran System Six model NSS 302, Thermo Electron). The samples were placed on a metallic stub using a carbon tape disc and the instrument worked at 6 kV.

Conclusions

In this work, we propose a new approach to preparing a nanostructured porous electrode with tunable features for glucose detection. We combine colloidal self-assembly, giving well-defined nanoporous IOs, with atomic layer deposition to precisely engineer the surface properties of the device and minimize the use of precious metals. This strategy enables us to create conductive electrodes while exploiting the attractive morphological properties of conventional IOs. We optimize the conductive AZO layer thickness to balance the transport of chemicals and electrode performance. We add Pt and a layer of GOx embedded in a polypyrrole matrix to form the biosensing unit. Our sensor is able to detect glucose concentrations below 1 nM, and it shows selectivity against pyruvate and gluconolactone as possible interferents in the biological fluids. The low limit of detection may open the possibility to detect glucose in body fluids with lower glucose concentration than blood, minimizing the discomfort for the patient. The compact, interconnected porous nature of the IOs may further integrate into microfluidic devices and thus provides an opportunity toward miniaturization.

Author Contributions

The manuscript was written through contributions of all authors. All authors have given approval to the final version of the manuscript. ‡These authors contributed equally.

Conflicts of interest

There are no conflicts to declare.

Acknowledgements

Notes and references

1 E. Gregg, J. Buckley, M. Ali, J. Davies, D. Flood, B. Griffiths, L.-L. Lim, J. Manne-Goehler, J. Pearson-Stuttard and J. Shaw, 2021.

2 J. Wang, *Chem. Rev.*, 2008, 108, 814–825.

3 S. B. Bankar, M. V. Bule, R. S. Singhal and L. Ananthanarayan, *Biotechnology Advances*, 2009, 27, 489–501.

4 V. G. Prabhu, L. R. Zarapkar and R. G. Dhaneshwar, *Electrochimica Acta*, 1981, 26, 725–729.

5 J. Kim, A. S. Campbell, B. E.-F. de Ávila and J. Wang, *Nat Biotechnol*, 2019, 37, 389–406.

6 N. Rohaizad, C. C. Mayorga-Martinez, M. Fojtů, N. M. Latiff and M. Pumera, *Chem. Soc. Rev.*, 2021, 50, 619–657.

7 M. C. Vestergaard, K. Kerman, I.-M. Hsing and E. Tamiya, Eds., *Nanobiosensors and Nanobioanalyses*, Springer Japan, Tokyo, 2015.

8 Z. Meng, R. M. Stolz, L. Mendecki and K. A. Mirica, *Chem. Rev.*, 2019, 119, 478–598.

9 J. Suthar, A. Alvarez-Fernandez, A. Taylor, M. J. Fornerod, G. R. Williams and S. Guldin, *ACS Appl. Nano Mater.*, 2022, 5, 12951–12961.

10 K. R. Phillips, G. T. England, S. Sunny, E. Shirman, T. Shirman, N. Vogel and J. Aizenberg, *Chem. Soc. Rev.*, 2016, 45, 281–322.

11 A. A. Saei, J. E. N. Dolatabadi, P. Najafi-Marandi, A. Abhari and M. de la Guardia, *TrAC Trends in Analytical Chemistry*, 2013, 42, 216–227.

12 A. Sarkar, A. B. Ghosh, N. Saha, G. R. Bhadu and B. Adhikary, *ACS Appl. Nano Mater.*, 2018, 1, 1339–1347.

13 S. Mishra, P. Yogi, P. R. Sagdeo and R. Kumar, *Nanoscale Res Lett*, 2018, 13, 16.

14 S. M. Usman Ali, O. Nur, M. Willander and B. Danielsson, *Sensors and Actuators B: Chemical*, 2010, 145, 869–874.

15 Z. Zhu, L. Garcia-Gancedo, A. J. Flewitt, H. Xie, F. Moussy and W. I. Milne, *Sensors*, 2012, 12, 5996–6022.

16 A. Harper and M. R. Anderson, *Sensors*, 2010, 10, 8248–8274.

17 R. B. Rakhi, P. Nayak, C. Xia and H. N. Alshareef, *Sci Rep*, 2016, 6, 36422.

18 N. J. Ronkainen, H. B. Halsall and W. R. Heineman, *Chem. Soc. Rev.*, 2010, 39, 1747.

19 A. Chamorro-Garcia and A. Merkoçi, *Nanobiomedicine*, 2016, 3, 184954351666357.

20 S. R. Chinnadayyala and S. Cho, *Nanomaterials*, 2020, 11, 37.

21 F. Chen, Y. Huang, R. Li, S. Zhang, B. Wang, W. Zhang, X. Wu, Q. Jiang, F. Wang and R. Zhang, *Chem. Commun.*, 2021, 57, 13448–13464.

22 J. E. S. van der Hoeven, A. V. Shneidman, N. J. Nicolas and J. Aizenberg, *Acc. Chem. Res.*, 2022, 55, 1809–1820.

23 C. Fenzl, T. Hirsch and O. S. Wolfbeis, *Angew. Chem. Int. Ed.*, 2014, 53, 3318–3335.

24 J.-H. Shin, J.-H. Kang, W.-M. Jin, J. H. Park, Y.-S. Cho and J. H. Moon, *Langmuir*, 2011, 27, 856–860.

25 E. Arsenault, N. Soheilnia and G. A. Ozin, *ACS Nano*, 2011, 5, 2984–2988.

26 M. J. Jara Fornerod, A. Alvarez-Fernandez, E. R. Williams, M. W. A. Skoda, B. Prieto-Simon, N. H. Voelcker, M. Stefik, M.-O. Coppens and S. Guldin, *ACS Appl. Mater. Interfaces*, 2022, 14, 56143–56155.

27 C. Huang, Y. Cheng, Z. Gao, H. Zhang and J. Wei, *Sensors and Actuators B: Chemical*, 2018, 273, 1705–1712.

28 Y. Pei, T. G. Molley and K. A. Kilian, *Macromol. Rapid Commun.*, 2020, 41, 1900555.

29 J. Wang, Y. Hu, R. Deng, R. Liang, W. Li, S. Liu and J. Zhu, *Langmuir*, 2013, 29, 8825–8834.

30 K. Pham, S. Pelisset, N. Kinnunen, P. Karvinen, T. K. Hakala and J. J. Saarinen, *Materials Chemistry and Physics*, 2022, 277, 125533.

31 K. P. Raymond, I. B. Burgess, M. H. Kinney, M. Lončar and J. Aizenberg, *Lab Chip*, 2012, 12, 3666.

32 B. Hatton, L. Mishchenko, S. Davis, K. H. Sandhage and J. Aizenberg, *Proc. Natl. Acad. Sci. U.S.A.*, 2010, 107, 10354–10359.

33 H. Cao, Y. Zhu, L. Tang, X. Yang and C. Li, *Electroanalysis*, 2008, 20, 2223–2228.

34 K. R. Phillips, T. Shirman, M. Aizenberg, G. T. England, N. Vogel and J. Aizenberg, *J. Mater. Chem. C*, 2020, 8, 109–116.

35 D. Karajz, D. Cseh, B. Parditka, Z. Erdélyi and I. Szilágyi, *J Therm Anal Calorim*, 2022, 147, 10259–10265.

36 Z. Wang, X. Li, H. Ling, C. K. Tan, L. P. Yeo, A. C. Grimsdale and A. I. Y. Tok, *Small*, 2018, 14, 1800395.

37 J. S. King, E. Graugnard and C. J. Summers, *Adv. Mater.*, 2005, 17, 1010–1013.

38 L. P. Bakos, D. Karajz, A. Katona, K. Hernadi, B. Parditka, Z. Erdélyi, I. Lukács, Z. Hórvölgyi, G. Szitási and I. M. Szilágyi, *Applied Surface Science*, 2020, 504, 144443.

39 L. Liu, S. K. Karuturi, L. T. Su and A. I. Y. Tok, *Energy Environ. Sci.*, 2011, 4, 209–215.

40 A. Ambrosi and M. Pumera, *ACS Catal.*, 2016, 6, 3985–3993.

41 V. O. Williams, E. J. DeMarco, M. J. Katz, J. A. Libera, S. C. Riha, D. W. Kim, J. R. Avila, A. B. F. Martinson, J. W. Elam, M. J. Pellin, O. K. Farha and J. T. Hupp, *ACS Appl. Mater. Interfaces*, 2014, 6, 12290–12294.

42 L. K. Tan, H. Gao, Y. Zong and W. Knoll, *J. Phys. Chem. C*, 2008, 112, 17576–17580.

43 J. Wang, G. Huang and Y. Mei, *Chem. Vap. Deposition*, 2014, 20, 103–111.

44 I. Alessandri, M. Zucca, M. Ferroni, E. Bontempi and L. E. Depero, *Small*, 2009, 5, 336–340.

45 K. Pham, H. Ali-Löytty, J. Saari, M. Zubair, M. Valden, K. Lahtonen, N. Kinnunen, M. Gunell and J. J. Saarinen, *Optical Materials*, 2022, 131, 112695.

46 A. Soldà, G. Valenti, M. Marcaccio, M. Giorgio, P. G. Pelicci, F. Paolucci and S. Rapino, *ACS Sens.*, 2017, 2, 1310–1318.

47 S. B. Hall, E. A. Khudaish and A. L. Hart, *Electrochimica Acta*, 1999, 44, 2455–2462.

48 Y. Zhou, C. L. Muhich, B. T. Neltner, A. W. Weimer and C. B. Musgrave, *J. Phys. Chem. C*, 2012, 116, 12114–12123.

49 R. L. Puurunen and W. Vandervorst, *Journal of Applied Physics*, 2004, 96, 7686–7695.

50 A. Goulas and J. Ruud van Ommen, *J. Mater. Chem. A*, 2013, 1, 4647.

51 J. Dendooven, R. K. Ramachandran, K. Devloo-Casier, G. Rampelberg, M. Filez, H. Poelman, G. B. Marin, E. Fonda and C. Detavernier, *J. Phys. Chem. C*, 2013, 117, 20557–20561.

52 M. Malferrari, A. Ghelli, F. Roggiani, G. Valenti, F. Paolucci, M. Rugolo and S. Rapino, *ChemElectroChem*, 2019, 6, 627–633.

53 S. A. Emr and A. M. Yacynych, *Electroanalysis*, 1995, 7, 913–923.

54 Y. Galvan, J. Bauernfeind, P. Wolf, R. Zarraga, M. Haumann and N. Vogel, *ACS Omega*, 2021, 6, 20956–20965.

55 E. Armstrong and C. O'Dwyer, *J. Mater. Chem. C*, 2015, 3, 6109–6143.

56 D.-J. Lee, H.-M. Kim, J.-Y. Kwon, H. Choi, S.-H. Kim and K.-B. Kim, *Adv. Funct. Mater.*, 2011, 21, 448–455.

57 B. Swatowska, W. Powroźnik, H. Czternastek, G. Lewińska, T. Stapiński, R. Pietruszka, B. S. Witkowski and M. Godlewski, *Energies*, 2021, 14, 6271.

58 P. Banerjee, W.-J. Lee, K.-R. Bae, S. B. Lee and G. W. Rubloff, *Journal of Applied Physics*, 2010, 108, 043504.

59 E.-H. Yoo and S.-Y. Lee, *Sensors*, 2010, 10, 4558–4576.

60 M.-C. Shin and H.-S. Kim, *Biosensors and Bioelectronics*, 1996, 11, 161–169.

61 D. Bélanger, J. Nadreau and G. Fortier, *Journal of Electroanalytical Chemistry and Interfacial Electrochemistry*, 1989, 274, 143–155.

62 S. De Zio, M. Becconi, A. Soldà, M. Malferrari, A. Lesch and S. Rapino, *Bioelectrochemistry*, 2022, 108343.

63 H.-P. Loock and P. D. Wentzell, *Sensors and Actuators B: Chemical*, 2012, 173, 157–163.

64 L. A. Currie, *Pure and Applied Chemistry*, 1995, 67, 1699–1723.

65 L. Xia, J. Song, R. Xu, D. Liu, B. Dong, L. Xu and H. Song, *Biosensors and Bioelectronics*, 2014, 59, 350–357.

66 C. Chen, Q. Xie, D. Yang, H. Xiao, Y. Fu, Y. Tan and S. Yao, *RSC Adv.*, 2013, 3, 4473.

67 R. M. DiSanto, V. Subramanian and Z. Gu, *WIREs Nanomed Nanobiotechnol*, 2015, 7, 548–564.

68 X. Guo, H. Li, H. Xu, S. Woo, H. Dong, F. Lu, A. J. Lange and C. Wu, *Acta Pharmaceutica Sinica B*, 2012, 2, 358–367.

69 D. Bruen, C. Delaney, L. Florea and D. Diamond, *Sensors*, 2017, 17, 1866.

70 N. Vogel, L. de Viguerie, U. Jonas, C. K. Weiss and K. Landfester, *Adv. Funct. Mater.*, 2011, 21, 3064–3073.

71 R. Schlitz, A. A. Amusan, M. Lammel, S. Schlicht, T. Tynell, J. Bachmann, G. Woltersdorf, K. Nielsch, S. T. B. Goennenwein and A. Thomas, *Appl. Phys. Lett.*, 2018, 112, 242403.